A New Deformation Enhancement Method Based on Multitemporal InSAR for Landslide Surface Stability Assessment

Youfeng Liu, Honglei Yang, Runcheng Jiao, Zeping Wang, Liuyu Wang, Wei Zeng, and Jianfeng Han

***Abstract*—The complex terrain and abundant ravines in the western mountainous areas of Beijing have led to dramatic changes in the geological environment. Monitoring and assessing the stability of landslide surfaces is of great significance for disaster prevention and ensuring the safety of the capital city. According to the spatial similarity characteristics of landslide surfaces, we propose a new interferometric synthetic aperture radar (InSAR) deformation enhancement method by taking into account the time-series deformation information of spatially adjacent homogeneous monitoring points. Taking Dongjiang Gully, Beijing as a typical study area, using multitemporal InSAR technology, 80 scenes of RADARSAT-2 data from September 2016 to September 2022 were processed to obtain their time-series surface deformation to verify the advantages of the proposed method. The results show that the standard deviation of the deformation difference of all monitoring points is generally reduced after the deformation enhancement, and the mean value is reduced from 5.1 to 3.3, which is 35.2% lower in comparison. Then this study assesses the stability of the landslide surface based on the deformation enhancement results. First, the optical image interpretation was combined with the angular distortions derived from deformation gradients to analyze the spatial location and boundaries of the landslide, and then to identify the infrastructure that is more susceptible to landslide impact. Second, through the principal component analysis method, the correlation between each component and the distribution characteristics of surface deformation was analyzed. Finally, starting from geological factors and triggering conditions, the driving force for landslide surface deformation was discussed, and it was drawn that seasonal precipitation is a major influencing factor. The proposed method can provide a reference for landslide monitoring and assessment in similar areas.**

***Index Terms*—Deformation enhancement, mountain landslide surfaces, multitemporal interferometric synthetic aperture radar (InSAR), stability assessment.**

Manuscript received 24 February 2024; revised 21 April 2024; accepted 28 May 2024. Date of publication 4 June 2024; date of current version 14 June 2024. This work was supported in part by the National Natural Science Foundation of China under Grant 42174026, and in part by the Beijing Key Laboratory of Urban Spatial Information Engineering under Grant 20220102. *(Corresponding author: Honglei Yang.)*

Youfeng Liu, Honglei Yang, and Zeping Wang are with the School of Land Science and Technology, China University of Geosciences, Beijing 100083, China (e-mail: jasonliuyf@163.com; hongleiyang@cugb.edu.cn; 447626218@qq.com).

Runcheng Jiao and Jianfeng Han are with the Beijing Institute of Geological Hazard Prevention, Beijing 100120, China (e-mail: 1012151216@cugb.edu.cn; 2012190023@cugb.edu.cn).

Liuyu Wang is with the Jiangsu Provincial Hydraulic Research Institute, Nanjing 210017, China (e-mail: wangly@cumt.edu.cn).

Wei Zeng is with the Chinese Society for Geodesy Photogrammetry and Cartography, Beijing 100830, China.

Digital Object Identifier 10.1109/JSTARS.2024.3409376

I. Introduction

AMONG the various geological disasters commonly seen in China, landslides generally have the highest frequency and are the most common type of geological disaster in mountainous areas [1]. Currently, it is slightly unfortunate that most of the landslides that have received much attention and study are located in southwestern China, and relatively few studies have been conducted on landslides in Beijing [2], [3], [4]. Beijing's mountainous areas account for approximately 62% of its total area. The western part consists of the Western Hills, which are a remnant of the Taihang Mountain range. This region is particularly susceptible to geological disasters such as landslides, mudslides, and landslide collapses. Among them, Dongjiang Gully has complex topographic features and developed faults, making it highly representative in the western hills of Beijing [5]. Additionally, seasonal precipitation and other triggering conditions may affect surface stability, leading to landslides that endanger roads and buildings and cause significant losses. Therefore, it is crucial to conduct deformation monitoring and stability assessments in this area.

With the advancement of space information technology, the methods of identifying and monitoring geological hazards, such as landslides, have changed tremendously [6]. Interferometric synthetic aperture radar (InSAR) remote sensing technology, which is not limited by factors such as season, time of day, and weather, and especially because of its wide monitoring range, has recently become one of the main technological tools in the field of observation of deformation of the terrain [7]. In 2000, Ferretti et al. [8] pioneered the concept of permanent scatterers (PS) and provided a complete data modeling and solution method in PSInSAR. Numerous scholars at both domestic and international levels adopted a large number of related techniques and theories to improve and extend the method in the following ten years, and finally formed the technical theory system of multitemporal InSAR [9], [10], [11], [12], [13]. In particular, multitemporal InSAR techniques such as small baseline subset InSAR (SBAS-InSAR) [14], temporarily coherent point InSAR (TCP-InSAR) [15], and SqueeSAR [16] have emerged. These multitemporal InSAR techniques measure large-scale surface deformation with millimeter-level accuracy and have been widely applied in the identification, investigation, monitoring, and risk assessment of seismic [17], landslide [18], [19] and other hidden dangers, and their advantages have been reliably

proven. For landslide areas dominated by mountainous terrain, PS-InSAR may lose coherence during long-term monitoring, while SBAS-InSAR and SqueeSAR technologies have more obvious advantages [20]. The distributed scatterer (DS) concept in SqueeSAR technology identifies statistically homogeneous pixels (SHP) with similar backscatter characteristics, making it capable of monitoring deformation on vegetated mountainous terrain [21], [22], [23].

Postprocessing of InSAR deformation monitoring results to make them more accurate and comprehensive for surface analysis is also a current research hotspot [24]. Most assessments of landslide surface deformation are based on InSAR results, with spatial location and extent of deformation determined by setting stability thresholds [21], [25]. However, it is difficult to determine a uniformly appropriate stability threshold because of the great inconsistency in the spatial and temporal deformation patterns and damage mechanisms of different landslides in the same or different regions. There is also the use of differential settlement of InSAR monitoring results to analyze the spatial extent of surface faults, cracks, and deformations [26], [27]. Additionally, from the perspective of long-term InSAR deformation monitoring data of all monitoring points within a study area, characteristics of the entire data matrix are analyzed using principal component analysis (PCA) [28], [29], [30], R/S analysis [31], and exponential models [32], [33] to assess surface deformation patterns and evaluate disaster risks. Previous studies have focused solely on evaluating deformation time series and comparing them with external triggering factors such as rainfall to assess landslide surface stability. In reality, landslide surfaces have relatively uniform features, primarily consisting of soil, rocks, and vegetation, and exhibit a certain degree of spatial similarity. Based on the time series, research that takes into account spatial similarity is still relatively limited [34]. Therefore, our new approach focuses on both temporal deformation changes and the spatial characteristics of such changes within a regional context, extending the work done previously. This represents a further step forward in assessing the stability of landslide surfaces.

In this study, we used multitemporal InSAR technology to process 80 C-band RADARSAT-2 data covering the Dongjiang Gully from 2016 to 2022, aiming to obtain information on landslide surface deformation. Using the time-series deformation results, we enhanced the InSAR deformation by taking into account spatial similarity, reducing the noise in the deformation signal, and providing higher-quality data for surface stability assessment. Then, based on the differential deformation of adjacent monitoring points, we analyzed the possible external edges of the landslide body. Meanwhile, we used PCA to analyze surface temporal deformation features. Finally, by combining the InSAR deformation monitoring results, we analyzed and discussed the possible influencing factors of landslide activity from both geological factors and triggering conditions. The research results can provide reference and guidance for landslide deformation monitoring and stability assessments in Dongjiang Gully and other similar mountainous areas.

II. Study Area and Data

A. Study Area

Dongjiang Gully is situated in the western mountainous area of Beijing. The administrative division belongs to Shijiaying Township, Fangshan District, Beijing, and is under the jurisdiction of Jinjitai Village. It ranges in longitude from 115°41′E to 115°43′E and in latitude from 39°52′N to 39°55′N, at an altitude of between 600 and 1600 m above sea level, with a gradual increase in elevation from south to north, and rugged terrain [Fig. 1(a)]. The study area is mainly distributed in the stratigraphic unit of the Lower Middle Jurassic Coal Yougou Formation, with shale and siltstone as the main rock types, and the fracture structure is developed, with a general NE trend and a dip angle of 50°–80° [Fig. 1(b)]. The climate type of the region is continental monsoon. The summer is hot and humid, which is the season with the most concentrated precipitation in a year, resulting in lush vegetation. The winter is relatively dry, with mainly snowfall, and the leaves fall and grasses dry up. Fig. 1(c) shows the normalized difference vegetation index (NDVI) data for the study area and it is seen that over a wide area, the NDVI values are greater than 0.4, indicating that the area is dominated by vegetation cover (https://app.climateengine.org/climateEngine). In contrast, NDVI values are lower in areas such as residential settlements and bare land.

By referring to the multitemporal InSAR monitoring results, a field survey was conducted along the mountain road to the deformation area, and slopes showing signs of slippage were visually observed and then photographed. After the field investigation, it was found that the area has high mountains, dense trees, winding roads, and a complex terrain and landscape environment. Fig. 2 shows the site photographs taken during the April 19, 2023, field reconnaissance, with specific locations labeled in Fig. 1(a). In addition, some obvious breaks and steep and gentle junctions are depicted (red dashed lines). It can be seen that the site is difficult to be monitored manually by traditional monitoring means such as level and total station, while some hidden ground cracks exacerbate the safety risk of manual monitoring and site investigation. The surface of the large-scale rolling steep hills is covered by vegetation, especially in the summer when the vegetation is dense, which also leads to the weak backscattering characteristics of the surface, and becomes a major obstacle for traditional remote sensing monitoring means. In addition, on the surface of steep slopes, the rock structure is relatively fragmented, and factors such as heavy rainfall are very likely to accelerate slope sliding, posing a safety threat to local buildings and personnel. To sum up, the geological environment in the study area is complex, with many hidden geological hazards, making it feasible and necessary to conduct monitoring, research, and analysis.

B. Data

This study uses the C-band RADARSAT-2 descending orbit SAR dataset collected by the Canadian Space Agency, which completely covers the study area with a range and azimuth

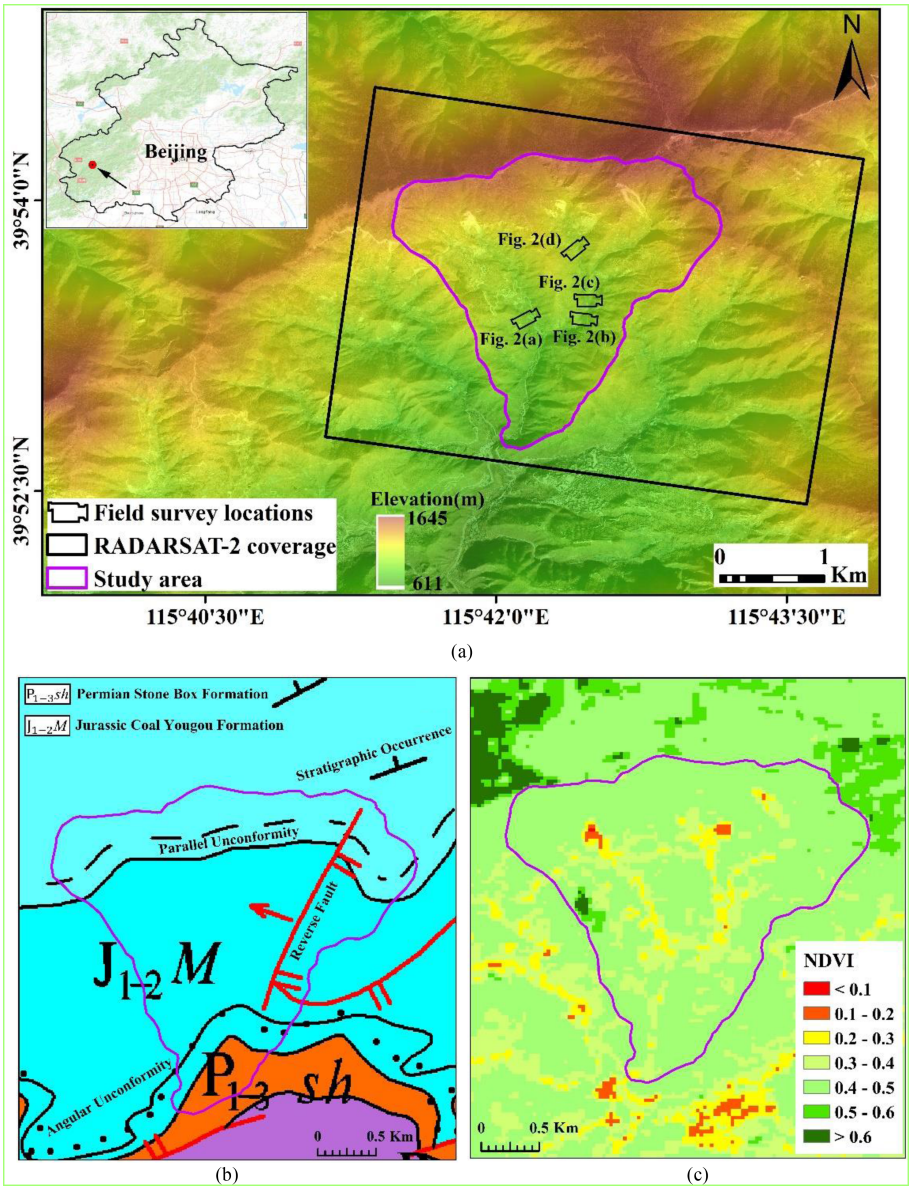

Fig. 1. Overview of the study area. (a) Coverage and geographic location. (b) Geological map (scale 1: 2 50 000 provided by the National Geospatial Advisory Committee of China). (c) NDVI distribution.

TABLE I
SAR IMAGE DATA PARAMETER INFORMATION

Parameters	Description
Polarization	HH
Wavelength (m)	0.0555
Incidence angle (deg)	45.42°
Heading (deg)	194.03°
Number of images	80
Time spans	2016/09/24-2022/09/17

resolution of 2.66 m and 2.48 m, respectively, and a 24-day revisit period. The 80 SAR images used in this study span from September 24, 2016 to September 17, 2022, with specific parameters shown in Table I. In addition, this study employed drone-based aerial survey technology to collect images of the study area and generated a high-precision digital elevation model (DEM) which has a ground resolution of 2.5 m. This DEM was used to geocode the SAR data and subtract the phase component related to terrain from the interferogram. Meanwhile, high-resolution photographic images are collected to illustrate detailed and intuitive landscapes.

The daily precipitation data for the research period can be downloaded from the European Centre for Medium-Range Weather Forecasts (ECMWF) database to assist in analyzing time-series deformation results.

III. METHODS

This study uses multitemporal InSAR to process RADARSAT-2 data and finally obtain the surface time-series

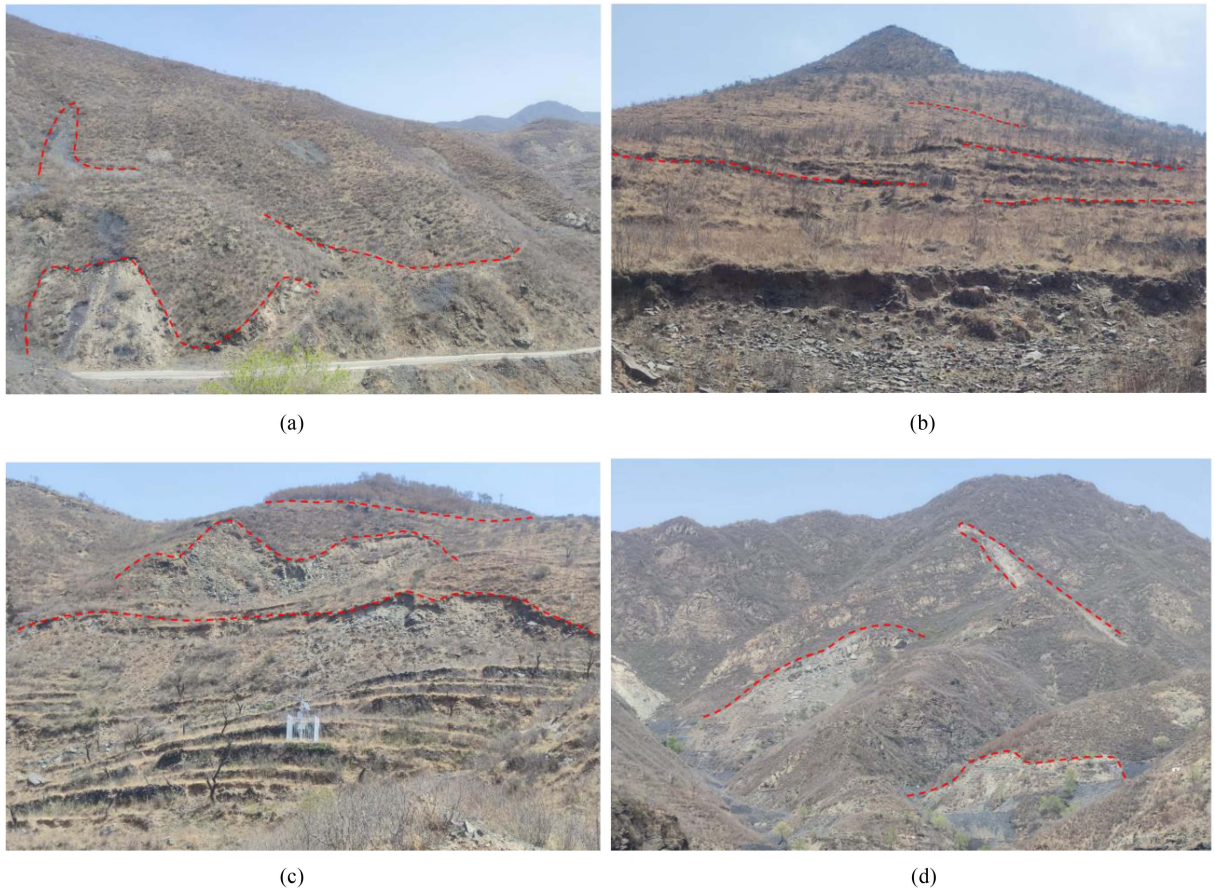

Fig. 2. (a)–(d) are photographic images of different locations, with their respective specific locations shown in Fig. 1.

deformation information. Then, the deformation results are enhanced from the spatiotemporal dimension. The landslide surface stability is evaluated using deformation difference and PCA methods, as shown in Fig. 3.

A. *Multitemporal InSAR Processing*

The widespread distribution of vegetation, the minimum 24-day satellite revisit period, and the interference of factors such as precipitation and human activities have seriously weakened the coherence of the interferograms. Therefore, we used the SqueeSAR method to select DS points and combined it with the SBAS technology to estimate surface deformation, with the aim of selecting as many monitoring points as possible while ensuring monitoring accuracy to meet the requirements of result analysis [22], [35]. Multitemporal InSAR processes RADARSAT-2 data in the GAMMA software, with multilooking using 1×1 (range $\times$ azimuth). The temporal baseline and spatial baseline thresholds are set to 96 days and 415 m, respectively, resulting in a total of 146 sets of interferograms. The phase of the *i*th interferogram is expressed as follows:

$$\Phi^i = \varphi^i_{ref} + \varphi^i_{top} + \varphi^i_{def} + \varphi^i_{atm} + \varphi^i_{noi} + 2k\pi \quad (1)$$

where φ_{ref},φ_{top},φ_{def}, φ_{atm}, and φ_{noi} are the reference ellipsoid phase, the topographic phase, the deformation phase, the atmospheric phase, and the noise phase, respectively; k is the ambiguity of the whole cycle. The reference ellipsoid phase can be calculated and removed based on the SAR imaging parameters and image slant distance. Topographic phases are then removed based on external DEM data. Gaussian filtering and NL-MMSE method [36] are used to optimize the phase of the interferogram sequence, improving its coherent signal and phase quality. Considering that the study area has a wide range of observations and significant height variations, the atmospheric phase is corrected by a linear regression model related to slant range and height.

$$\varphi^i_{atm} = a_0 + a_1 * r + a_2 * r * \Delta h \quad (2)$$

where a_0, a_1, a_2 are the coefficients; r is the slant range between the radar and the point target; Δh is the height difference between the point target and the reference point. In the SqueeSAR, the hypothesis test of confidence interval (HTCI) algorithm is applied to identify the SHP of each pixel in the image based on the temporal amplitude information [37], [38]. The number of SHP is counted, and then a certain threshold is set, and those greater than this threshold are defined as DS candidate points (DSC). Phase optimization of the interferogram sequence is performed based on DSC, and its quality is evaluated by the

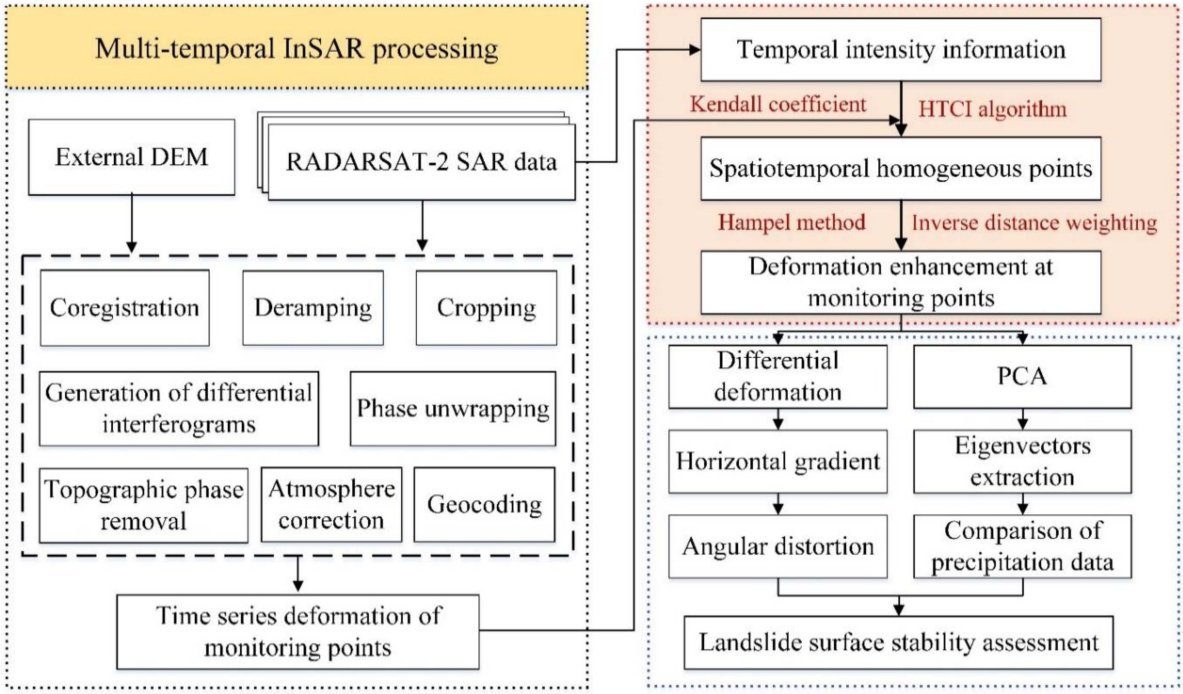

Fig. 3. Flowchart of multitemporal InSAR processing and landslides stability assessment.

temporal coherence value γ.

$$\gamma = \frac{1}{M}\mathrm{Re}\sum_{nk=1}^{M} e^{i\phi_{nk}} e^{-i\hat{\phi}_{nk}} \tag{3}$$

where ϕ_{nk} is the original interferogram, $\hat{\phi}_{nk}$ is the optimized interferogram, and M is the number of interferogram. We consider DSC with temporal coherence greater than 0.4 as the final DS. To further improve the selection quality of monitoring points, we use the amplitude difference index less than 0.4 to select PS. It should be noted that in the predominantly mountainous study area, the number of selected PS is usually small and it is hard to satisfy research requirements. Therefore, this study will jointly select DS and PS as monitoring points. The minimum cost flow method is applied to unwrap the phases of the monitoring points, and then the unwrapped phases are filtered in the spatial and temporal domains to attenuate the impact of atmospheric delay and noise. Finally, the time-series deformation of the monitoring point is derived through singular value decomposition (SVD).

B. InSAR Deformation Enhancement

Considering that mountainous areas have simpler landforms compared to urban areas, they exhibit spatial similarity within a nearby area. Currently, the analysis of InSAR deformation mostly focuses on the monitoring results of individual monitoring points, neglecting the spatial relationships between them. Therefore, based on the resolution of the SAR data and prior experience, we set a neighboring window for the central monitoring point, select spatial and temporal homogeneous monitoring points within the window, and then use spatial inverse distance weighting (IDW) to enhance the time-series deformation of the central monitoring point. By conducting InSAR deformation enhancement, we can reduce noise while maintaining spatial consistency in deformation.

Fig. 4 shows the schematic diagram of InSAR deformation enhancement. Within a certain window, the monitoring points are first screened in the spatial dimension based on the distribution of the center point's SHP. Then, in the temporal dimension, the Kendall correlation coefficient is calculated to further filter the monitoring points [39]. IDW is applied to the remaining monitoring points to enhance the time-series deformation of the central monitoring point. Additionally, to prevent sudden noise or abnormal values in the time series deformation, we use the Hampel method to detect and filter out the center monitoring point, completing the deformation enhancement [40].

The HTCI algorithm utilizes temporal amplitude information to compare the similarity between the center point and neighboring points within the window, and selects homogeneous points based on the idea of hypothesis testing in statistics. Assuming that SAR image intensity sequence (I) obeys Rayleigh distribution (4), and the variance of random variables is $\sigma^2/2$. By the property that the coefficient of variation (CV) of the Rayleigh distribution is constant, for radar data with multilook L, $CV \approx 0.52/\sqrt{L}$. Settings $\hat{\mu}_{cen}(p)$ and $\hat{\mu}_{neig}$ are the average values of the temporal amplitudes of the reference pixel p and its neighboring pixels, respectively. Relative to the center point, if the samples of neighboring points within the window satisfy the given confidence interval α, they are considered to be SHP

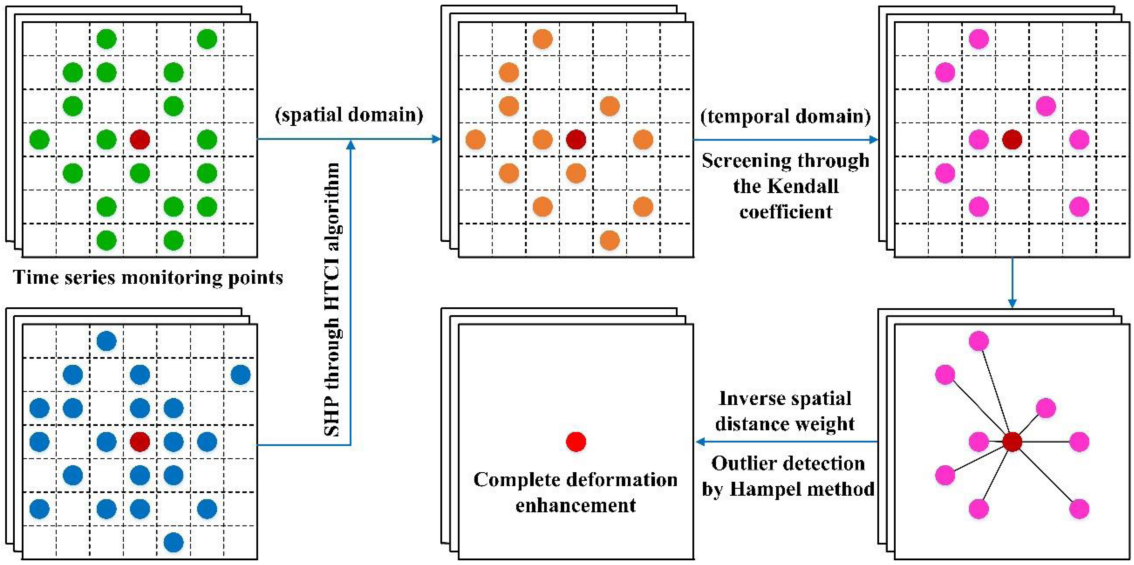

Fig. 4. Schematic diagram of InSAR deformation enhancement. (Assume that in a 7 × 7 window, the dark red solid circle represents the central monitoring point, the green and dark red solid circles represent the distribution of all monitoring points, the blue solid circle represents the SHP distribution of the central monitoring point, the orange solid circle represents the point that is both the monitoring point and the SHP, and the magenta solid circle represents the point further screened by Kendall coefficient, and the central monitoring point is finally represented as an orange solid circle after the deformation enhancement.).

of the center point (5) [41], [42].

$$f(I) = \frac{1}{\sigma^2} e^{-\frac{I}{\sigma^2}}, I \geq 0 \tag{4}$$

$$P\left\{\hat{\mu}_{cen}(p) - z_{1-\alpha/2} \cdot 0.52 \cdot \hat{\mu}_{cen}(p)/\sqrt{N \cdot L} < \hat{\mu}_{neig} < \cdots \right.$$

$$\left. \hat{\mu}_{cen}(p) + z_{1-\alpha/2} \cdot 0.52 \cdot \hat{\mu}_{cen}(p)/\sqrt{N \cdot L}\right\} = 1 - \alpha. \tag{5}$$

The Kendall coefficient belongs to the statistical theory that is used to calculate the degree of correlation between multiple ranked variables. Because surface deformation is continuous in time and within a small range, its overall trend is usually monotonic and similar, so this coefficient can be used to calculate the temporal deformation correlation between monitoring points. The calculation formula is as follows:

$$Ken = \frac{C - D}{\sqrt{(N_3 - N_1)(N_3 - N_2)}}$$

$$N_1 = \sum_{i=1}^{s} \frac{1}{2} U_i(U_i - 1); N_2 = \sum_{i=1}^{s} \frac{1}{2} V_i(V_i - 1);$$

$$N_3 = \frac{1}{2} N(N-1). \tag{6}$$

In the formula, *C* represents the number of deformation values that are consistent between the central point and neighboring points, while *D* represents the number of inconsistent deformation values. N_1 and N_2 are calculated based on the temporal deformation of the center point and the neighboring points, respectively. Taking N_1 as an example, the same deformation values in the temporal deformation of the center point are combined into a small set, where s represents the number of small sets and U_i represents the number of deformation values contained in the ith small set. Similarly, N_2 is calculated based on the temporal deformation of the neighboring points. The value of Ken ranges from -1 to 1, and the closer its value is to 1, the more consistent the deformation between the center point and the neighboring points. In this study, points with a Kendall coefficient greater than 0.6 are considered to be spatiotemporal homogeneous. Then, calculate its IDW, such that.

$$w_{IDW} = h_i^{-1} \Big/ \sum_{p=1}^{N_P} h_i^{-1}. \tag{7}$$

w_{IDW} is determined by *h* (Euclidean distance), which is calculated by the center point and the spatiotemporal homogeneous points; N_p is the number of spatiotemporal homogeneous points.

The Hampel method uses a sliding window to detect the time-series deformation value of the central monitoring point after IWD. First, take a window of odd length, then calculate the median of the samples within the window. Use the absolute median to estimate the standard deviation of each sample from the median. A threshold is set using a multiple of the standard deviation, and when a sample value differs from the median by more than the threshold, that sample value is considered an outlier and replaced with the median. The setting of the window size depends on the time interval of the SAR data. Based on processing experience, SAR data with a longer time interval should be assigned a smaller window size to avoid increasing detection errors across seasons or years [40]. On the other hand, SAR data with a shorter time interval can have a larger window size to avoid missing short-term anomalies. Based on the multiple of the standard deviation to set the threshold, the quality of outlier detection can be controlled. By setting a lower threshold, the filtering standard becomes more stringent, making it easier to identify more outliers. In this study, the size of the sliding window is defined as 5, representing a period of approximately

120 days, with quarterly sliding units to minimize cross-seasonal detection errors, and empirically, a standard deviation of 2 times is set as a more appropriate threshold.

C. Landslide Surface Stability Assessment

According to III-B, in mountainous areas with spatial similarity, the deformation enhancement method is essentially an optimization of deformation monitoring results. Its purpose is to provide higher-quality monitoring results for subsequent surface deformation analysis, stability assessment, deformation prediction, and other related studies. Thus, the assessment of landslide surface stability in this section is based on the results obtained after deformation enhancement, which also serves as a test for the deformation enhancement method.

1) Differential Deformation and Angular Distortions: The slowly moving landslide surface, which occurs year-round, is the most suitable monitoring target for the time-series InSAR technique. It has significant deformation differences compared to the stable rock and soil surface around it, especially at the boundary. Based on the spatial deformation patterns of the surface, at the boundary of a landslide, tension cracks or misalignment often form, resulting in significant differential deformation. Therefore, the deformation difference (gradient) between monitoring points can be calculated to analyze and map the boundaries of the landslide. The high gradient determines the sudden change in deformation patterns, thus identifying the area with the most significant horizontal stress. Therefore, for the stability assessment of surface deformation, information on deformation gradients can be used in addition to deformation rates or accumulated deformation. The gradient of a deformation between two points is defined as the ratio of the differential deformation variable ΔdU to the horizontal distance l [27], [33].

$$h_U = \frac{\Delta dU}{l}. \tag{8}$$

Then, the inverse tangent function of the horizontal gradient is used to derive the angular distortion β.

$$\beta = \arctan h_U. \tag{9}$$

The calculated value of h_U is dimensionless and presented as a percentage; the unit of β is given in degrees. The larger the angular distortion β values, the more significant the deformation within a short distance, which is most likely the sliding boundary of the landslide. First, we convert the cumulative deformation from LOS direction to vertical direction based on the radar incidence angle and use it as the input value. Then, we calculate the difference in cumulative deformation between the central monitoring point and the surrounding eight monitoring points. The horizontal gradient of the central monitoring point is also derived from the horizontal distance. In this way, there can be a maximum of eight horizontal gradient values, and we select the maximum value as the horizontal gradient of the central monitoring point. We then derive the angular distortion values for all monitoring points. Finally, based on the spatial distribution characteristics of β value, combined with optical images and visual interpretation results, we evaluate and analyze the stability of landslide surfaces.

2) Spatiotemporal PCA: Time-series deformation monitoring data often contain different components, and time series decomposition is a commonly used data processing strategy. In this article, the PCA method reduces the effective dimensionality of the dataset while maintaining the characteristics of the data, and concentrates the data information in a small number of principal components. We implement PCA using the SVD of the time-series deformation data matrix.

$$P = XW \tag{10}$$

$$X = U\Sigma W^T. \tag{11}$$

X is the matrix of time-series deformation for $m \times n$, where m is equal to the number of monitoring points and n is equal to the number of time series data [30]. After performing SVD on X, we obtain three matrices U, Σ and W, where U and W are orthogonal matrices. W is the eigenvector of the data covariance $X^T X$, where T denotes transpose. Σ is a diagonal matrix, whose diagonal elements are the singular values. These singular values reflect the characteristics of the original matrix X, especially in data compression and noise reduction. The magnitude of the singular values indicates the importance of each component, and different singular values will correspond to different intensities of the scattering signal. P is the score matrix of principal components (PCs) with m rows and n columns. Therefore, the score map of P and the eigenvector of W characterize the temporal and spatial features of the deformation results, respectively. Arranged by the magnitude of eigenvalues, the cumulative contribution rate of the first six PCs reached 87%, indicating a relatively high proportion. Based on experience, the first six PCs are retained for analysis in this study, ignoring subsequent components that may represent tropospheric artifact turbulence or other noise.

IV. Results and Discussion

A. Deformation Monitoring Results

Multitemporal InSAR ultimately obtained 3 92 333 monitoring points, with a high distribution density that can provide detailed information on the deformation distribution characteristics of the surface. Fig. 5(a) shows the results of deformation rate in geographic coordinate system. In order to mitigate long-wave noise, we picked a phase unwrapping reference point in the relatively stable residential area and obtained the minimum rate value of −45.2 mm/yr and the maximum rate value of 36.3 mm/yr through inversion. The deformation rate is mostly within the range of −15–15 mm/yr, indicating that most of the surface in the study area is relatively stable, with some sporadic deformation areas. Among them, several landslide bodies are obvious. In order to gain a more precise insight into the deformation characteristics of the landslide surface, we selected two of the obvious deformation areas, as shown in Fig. 5(a) as 1# and 2#. In terms of landslide monitoring results, landslide areas generally have low NDVI values, indicating that the surface of the landslide bodies has less vegetation and is mostly dominated by bare rock and soil. Furthermore, considering the complex field environment, it is difficult to use traditional ground measurement methods to collect external measurement data for

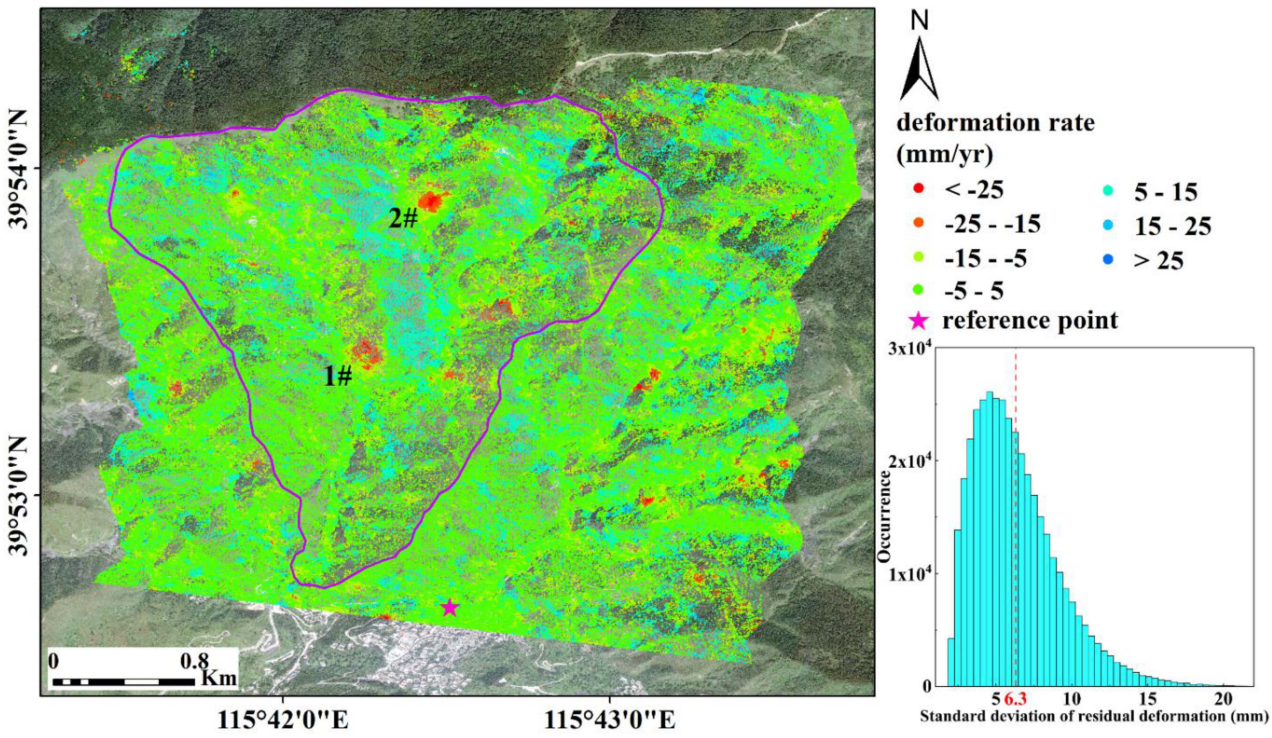

Fig. 5. (a) Deformation rate results and (b) standard deviation result statistics for accuracy verification.

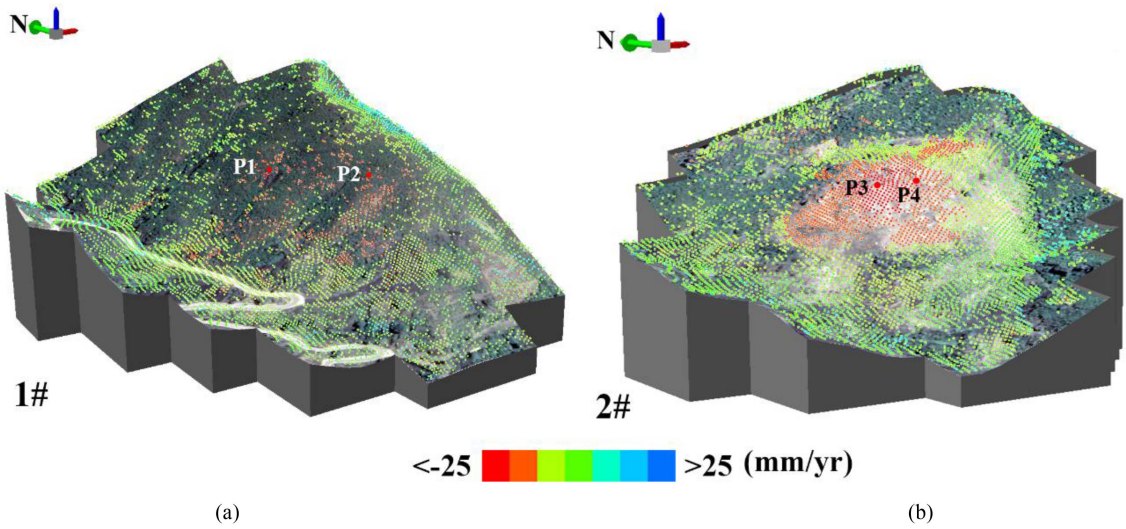

Fig. 6. 3D visualization of the InSAR results. (a) 1# area. (b) 2# area.

accuracy verification. Therefore, in this study, the internal accord accuracy of the monitoring results is verified using the residual deformation standard deviation index caused by factors such as atmospheric delay and baseline error, which in turn illustrates the reliability of the monitoring results. The standard deviation result statistics show [Fig. 5(b)]: the calculated values of all monitoring points are mainly concentrated within 10 mm, with an average value of 6.3 mm. The internal accord accuracy of the results is at the millimeter level, indirectly verifying the reliability of the monitoring results.

Next, we will focus on the analysis and discussion of the 1# and 2# landslide areas. Fig. 6 is a three-dimensional visual representation of the 1# and 2# landslide areas, where the color variations of the monitoring points are consistent with the color changes in Fig. 5(a). It can be visually observed that both landslides exhibit the most significant deformation in the middle

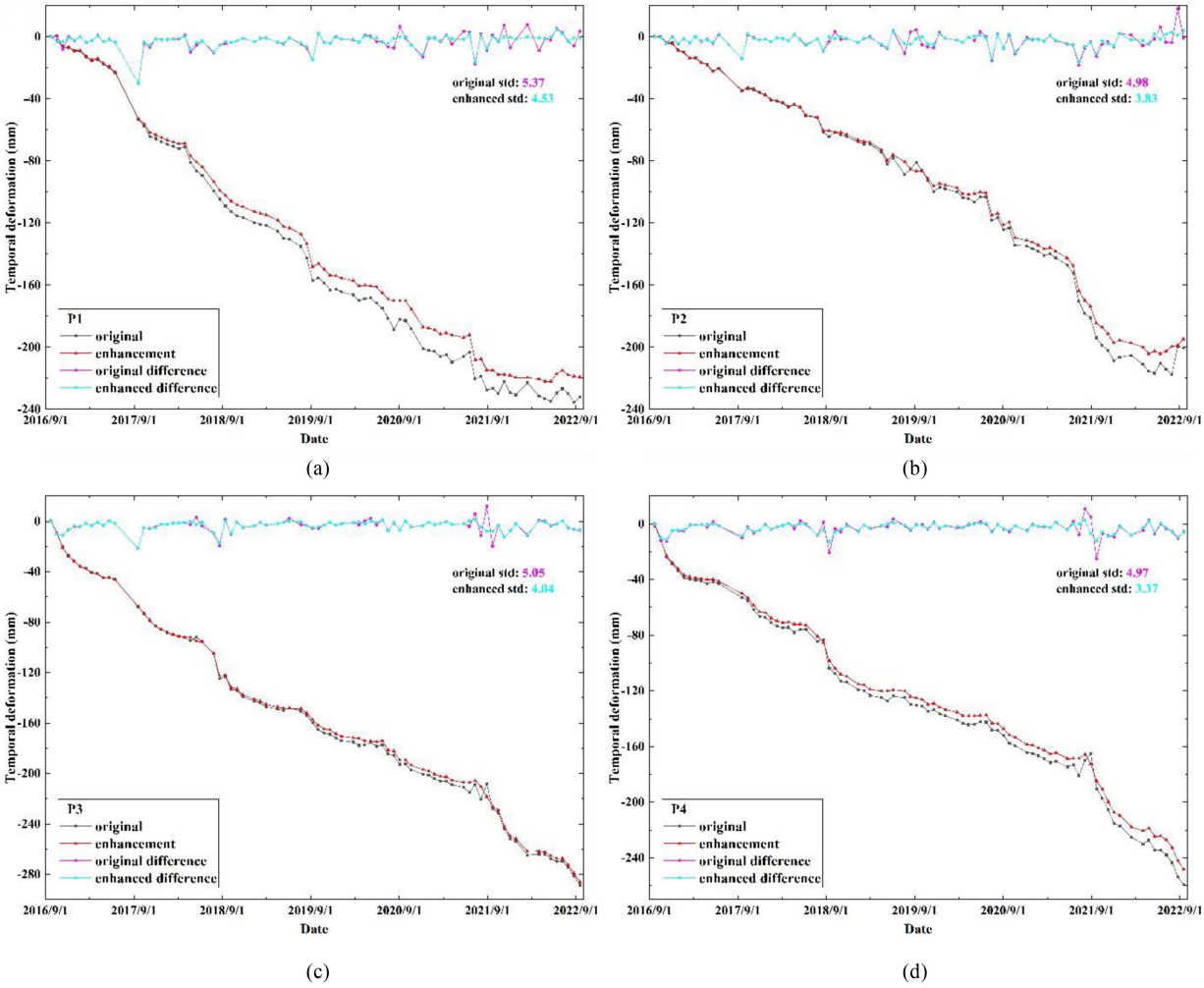

Fig. 7. (a), (b), (c) and (d) denote the temporal variation before and after deformation enhancement of the P1-P4 feature points, respectively.

section of the slope, with deformation rates over −20 mm/yr. In addition, the 1# area has a minimum elevation of 812 m and a maximum elevation of 1052 m, resulting in a slope height difference of approximately 240 m. The slope angle in the deformed area of the middle section is around 40°. The 2# area has a minimum elevation of 1010 m and a maximum elevation of 1275 m, resulting in a slope height difference of approximately 265 m. The slope angle in the deformed area of the middle section is around 37°. Both areas have high and steep terrain, and the 1# area is situated adjacent to the road, making it susceptible to blockage if surface deformation accelerates, which would impact normal production activities.

We selected two feature points at different geographical locations within the deformation areas of 1# and 2#, named P1, P2, P3, and P4, respectively (Fig. 6), to exhibit their time-series deformation patterns after deformation enhancement. At the same time, it is compared with the original deformation to verify the necessity and reliability of deformation enhancement. Fig. 7(a)–(d) corresponds to the deformation change direction of points P1–P4 from 24 September 2016 to 17 September 2022, respectively. The black line represents the original time-series deformation trend; the red line represents the time-series deformation trend after deformation enhancement; the pink line represents the difference between the original time-series deformation at adjacent time periods; and the blue line represents the difference between the time-series deformation after deformation enhancement at adjacent time periods. After InSAR deformation enhancement, the temporal deformation trend is smoother, and some deformation jumps have been corrected. We use the standard deviation of the deformation difference before and after deformation enhancement to quantitatively evaluate the effect. The standard deviation of the P1 decreased from 5.37 to 4.53, that of the P2 from 4.98 to 3.83, that of the P3 from 5.05 to 4.04, and that of the P4 from 4.97 to 3.37, which were 15.6%, 23.1%, 20.0%, and 32.2% lower year-on-year, respectively. The decrease in the standard deviation values indicates a decrease in the magnitude of deformation change under adjacent time, which in turn indicates a smoother time-series deformation trend. Finally, after deformation enhancement, the cumulative deformation values of P1, P2, P3, and P4 were −219.2 mm, −194.7 mm, −285.9 mm, and −248.3 mm, respectively.

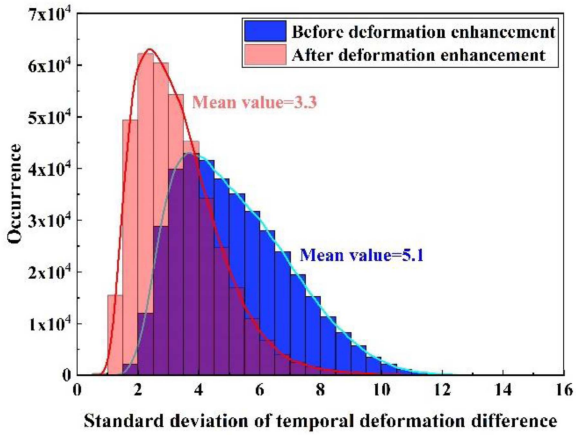

Fig. 8. Standard deviation statistics of the deformation difference values for all monitoring points.

While conducting quantitative analysis on the four feature points, we also calculated the standard deviation of deformation difference for all monitoring points before and after deformation enhancement, in order to better observe the deformation enhancement effect (Fig. 8). Before deformation enhancement, the minimum value of standard deviation is 1.3, the maximum value is 15.7, and the average value is 5.1; after deformation enhancement, the minimum value of standard deviation is 0.8, the maximum value is 13.9, and the average value is 3.3. Obviously, after the deformation enhancement, the mean value was reduced by 1.8, compared with a 35.2% reduction, indicating that the time-series deformation values at all monitoring points were effectively removed or corrected for anomalies, and the time-series deformation trend was smoother. This further proves the necessity and reliability of deformation enhancement. We will use the time-series deformation results after deformation enhancement for subsequent discussion on the landslide surface.

B. Landslide Surface Stability Discussion

1) Angular Distortions: The spatial distribution of the angular distortion β values estimated from vertical cumulative deformation is shown in Fig. 9. A higher β value indicates a more significant difference in deformation between adjacent monitoring points in space. During the study period, the areas with larger deformation rate and cumulative deformation are reflected in the angular distortion β values. The β values of several landslide bodies in the study area reached 0.067° or higher, indicating a deformation difference of over 5 mm at a distance of about 3 m. Through the β values, the spatial differences in surface deformation can be more clearly observed, potential landslides can be discovered, and possible external boundaries of landslide bodies can be mapped.

We focused on analyzing the β value distributions of 1# and 2# landslide bodies and found that: the center region of 1# landslide body had the highest β value, which gradually decreased with increasing distance from the center, indicating a large spatial deformation difference throughout the area; the high β value of 2# landslide body showed an approximate closed-loop spatial pattern, indicating that the spatial deformation difference in the center of the landslide body is small, while the high β values around the center precisely reflect its external edge. In the enlarged views of landslides 1# and 2#: the white dashed line represents the outer contour shown by the optical image, and the red closed solid line indicates the deformation boundary plotted according to the β value (Fig. 9). The outer boundary of the solid red line essentially coincides with the boundary of the dashed white line. However, the red solid line is not as large in extent as the white dashed line, indicating that deformation has weakened in some areas of the landslide body. In turn, we can determine which part of the landslide body has stabilized and which part is still undergoing significant deformation. After calculation, the deformation areas of 1# and 2# landslide bodies are approximately 17.3×10^3 m^2 and 8.8×10^3 m^2, respectively. By identifying edges, it is possible to capture the deformation development of landslides, determine which infrastructure is more vulnerable to the impact of the landslide, and provide information for the prevention and control of local geological disasters.

2) Deformation Feature Extraction With PCA: Fig. 10 displays the spatial response scores of the first six PCs. The score map of PC1 is more closely related to the distribution characteristics of surface deformation, with strong spatial consistency. In Fig. 5(a), in the area where the deformation rate is negative, then PC1 score also shows negative values, with a maximum value of −1817; in the area where the deformation rate is positive, the PC1 score shows positive values, with a maximum value of 1346. This indicates that the deformation rate value is positively correlated with the PC1 score value, and the range of PC1 score values is much larger than the rate, so the deformation area is more significant in the PC1 score map. From the score values, it can be seen that PC1 accounts for about 61% of the overall deformation signal, indicating that it is related to the time series deformation. The PC3 score has a high similarity to the PC1 score, showing a spatially correlated signal consistent with the deformation results. Unlike the PC1 score, it is not correlated in time (Fig. 11). PC3 may be mainly related to residual orbital errors. The spatial consistency between PC2 score and deformation results is slightly present but not significant, and there is also no temporal correlation. This may be influenced by a combination of residual orbital errors, and/or turbulent tropospheric artifact and/or noise. On the contrary, the scores of PC4, PC5, and PC6 are not spatially correlated with the deformation results, and their eigenvectors randomly fluctuate around zero over time. Moreover, there is no significant correlation between the score distribution and terrain, which may be related to turbulent tropospheric artifact and/or noise.

Score maps can be converted to deformations by multiplying the corresponding eigenvectors at a given time, as shown in Fig. 11. The PC1 scores of the points P1–P4 all show an approximate linear trend over time [Fig. 11(a)], indicating that the signal has a high degree of temporal correlation. We also collected precipitation data during the study period for auxiliary analysis, which is represented by the pink bars in Fig. 11. The time-series deformation of the PC1 eigenvector shows small fluctuations with increasing precipitation, especially in 2018,

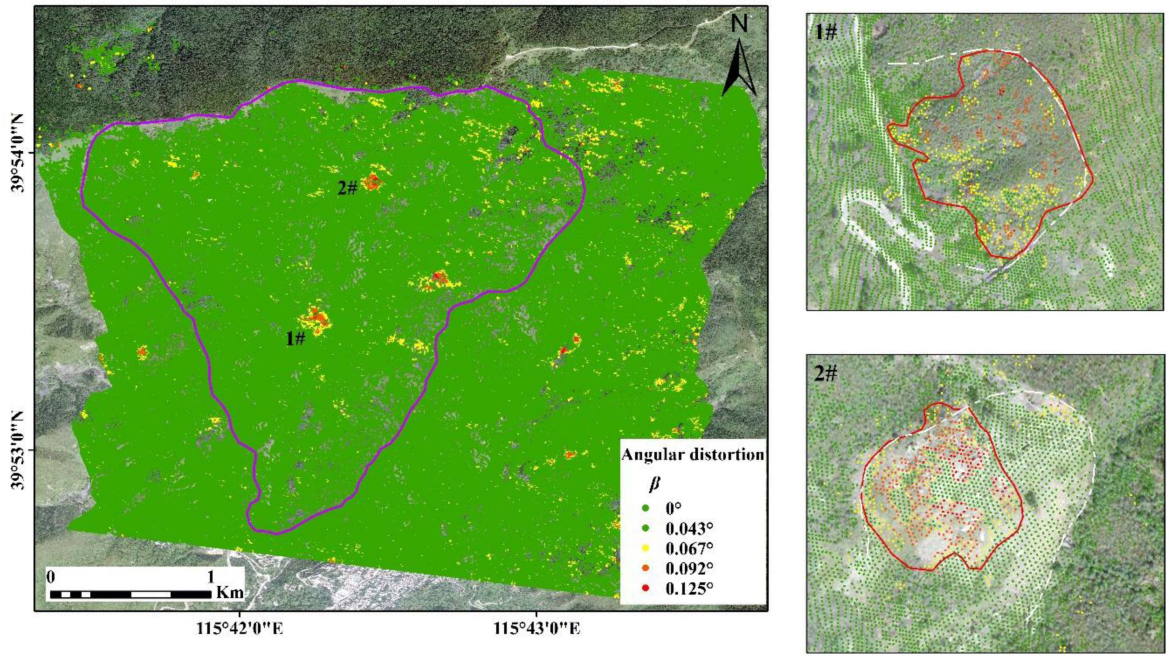

Fig. 9. Angular distortion obtained from the difference of deformation results.

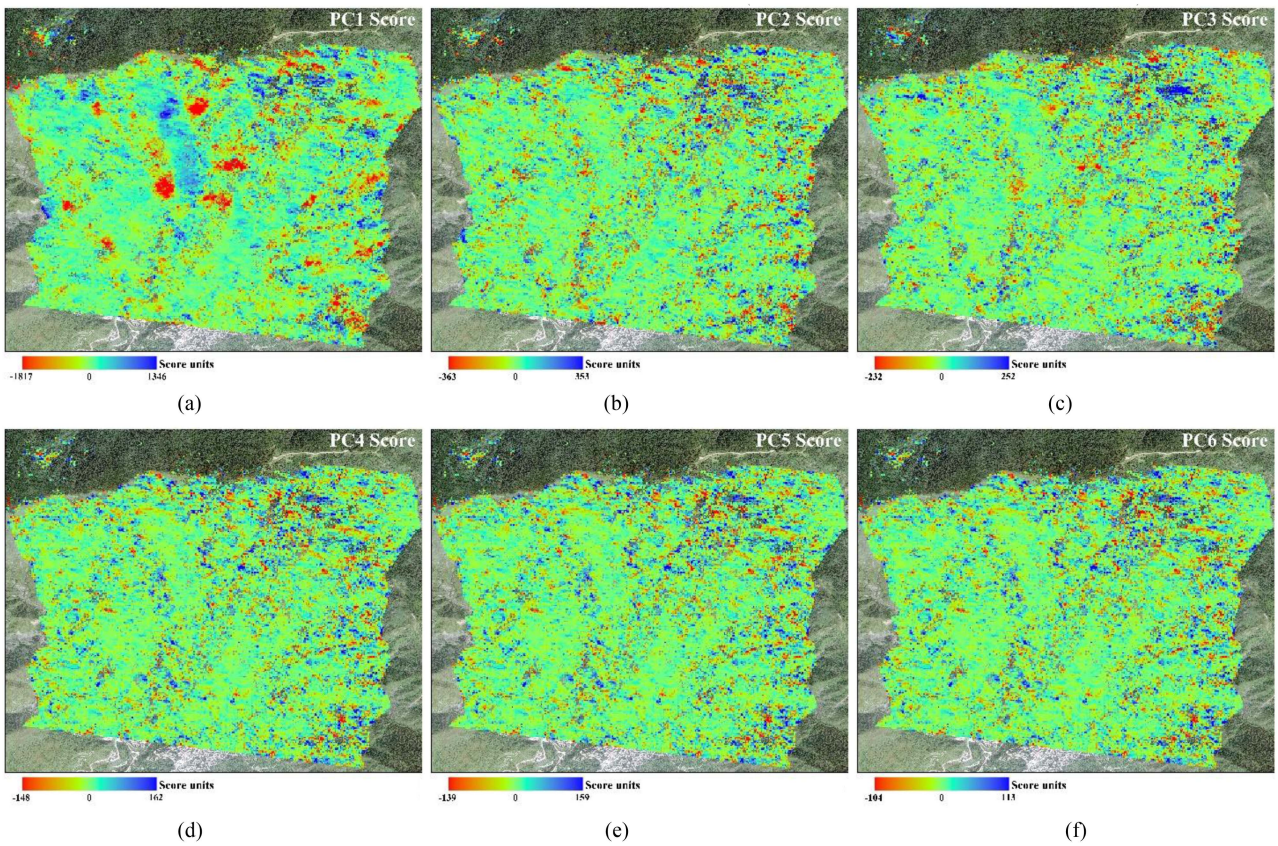

Fig. 10. (a)–(f) Score maps for components PC1-PC6 in sequence.

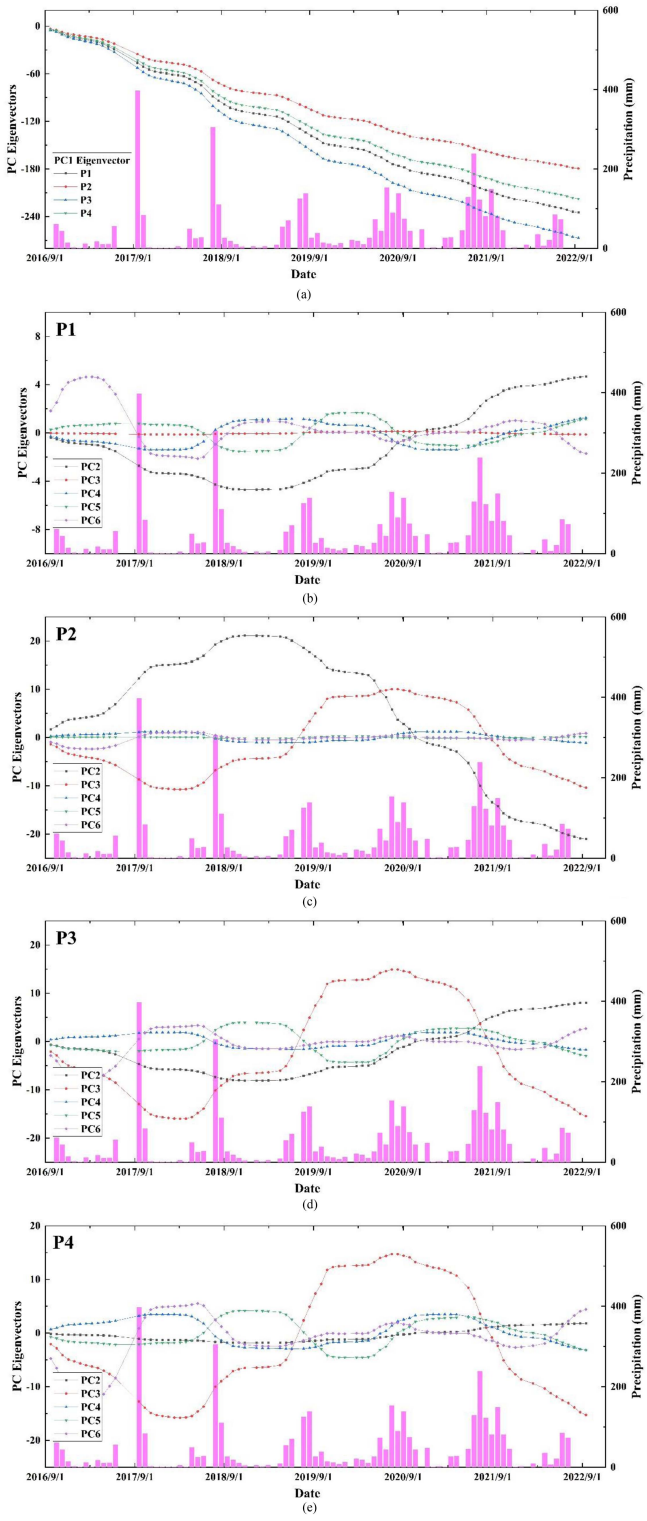

Fig. 11. PCA characterization of surface deformation. (a) PC1 eigenvectors of points P1–P4. (b)–(e) PC2–PC6 eigenvectors of points P1–P4.

2019, and 2020. This indicates that increased summer precipitation is one of the main factors affecting deformation. For other PC eigenvectors: the PC2 eigenvector shows the most significant time-series deformation signal at point P1; PC2 and PC3 eigenvectors show the most significant time-series deformation signal at point P2; PC3 eigenvector shows the most significant time-series deformation signal at points P3 and P4. Like the PC2 or PC3 eigenvectors, which are more or less consistent with the surface deformation distribution in space and show a stronger signal in time series, this signal may be mainly related to the residual orbital errors, atmospheric delay errors, and other factors. No matter which kind of space-borne SAR data is applied, these errors are difficult to completely eliminate. In addition, the deformation signals of PC3–PC6 eigenvectors may mainly be caused by noise. Unfortunately, except for the PC1 eigenvector, there is no consistent change rule for all PC eigenvectors' time-series deformation signals, so it is difficult to express them with a clear model.

C. Driving Force of Landslide Surface Deformation

According to the results of the deformation rate and temporal deformation in the study area, deformation is found to occur to varying degrees in the reservoir basin, reservoir bank, and surrounding vegetation areas. The analysis of the results, combined with the field survey, revealed that the factors affecting surface deformation fall into two main categories: natural geography and man-made activities. Sudden large-scale deformation, such as collapse, is mainly influenced by natural geographical factors, while slow small-scale deformation, such as slip, is mainly influenced by man-made activities.

1) The topography of the study area is characterized by gullies and ravines, with typical "V" shaped valleys. According to the survey, the area is about 3.87 km^2, with an average slope of 31.8° and a relative height difference of about 1000 m [Fig. 1(a)]. In addition, the rock types in the area are mainly shales and siltstones with soft rock quality [Fig. 1(b)]. Since geological factors, such as topography and geological structure, determine the degree of susceptibility to geological disasters, areas with such topography and geological conditions are prone to geological disasters, such as landslides and mudslides.
2) The hot and rainy summer in the study area is the most concentrated precipitation season in a year. From 2016 to 2022, although the time-series deformation trend shows an approximate linear change, it has also shown a slight acceleration fluctuation due to the increase in summer precipitation each year [Fig. 11(a)]. In addition, in the past 20 years, there have been several earthquakes of magnitude 1–2 in the Western Hills of Beijing, but there have been no reports of geological disasters caused by micro-earthquakes. This indicates that the landslide surface in the Western Hills of Beijing is currently in an approximate linear deformation stage, with a low probability of sudden natural disasters such as earthquakes. In addition, according to the monitoring results [Fig. 5(a)] and NDVI distribution [Fig. 1(c)], the surface of the landslide deformation areas has less vegetation and is mostly dominated by bare rock and soil. This geomorphological feature, accompanied by seasonal precipitation, becomes one of the main influencing factors for its deformation.

3) The history of coal mining in the study area is nearly a thousand years, with numerous small coal mines. The serious lack of information on underground mining scope, mining depth, and mining thickness has always been a difficulty in the investigation and research of subsidence in the area. Fortunately, mining activities in the study area stopped in 2008, and there has been no other human engineering activity interference since then. In addition, the deformation areas in the deformation rate results are distributed in a spotty pattern, with a high degree of distinction from stable areas, and no large-scale surface subsidence has been detected. Given that mining activities have ceased for more than ten years, it is concluded that human activities such as coal mining have a relatively small impact on the surface deformation of the landslide.

Generally, geological disasters are the result of the coupling of geological factors and induced conditions. We discuss the stability of landslide surface deformation in terms of geological factors such as topography and geological composition, induced conditions such as precipitation and human activities, and combined with the InSAR deformation monitoring results, which can help to scientifically and comprehensively understand the risk of landslide surface risks.

V. Conclusion

In this study, multitemporal InSAR technology was employed to process 80 scenes of RADARSAT-2 data, overcoming the limitations of traditional InSAR technology, such as sparse monitoring point distribution and poor interference quality resulting from time decorrelation. Considering the spatial and temporal relationship between monitoring points, the InSAR deformation was enhanced. After the deformation enhancement, the standard deviation of the deformation difference between each monitoring point was effectively reduced, and the temporal deformation trend became smoother. By using two typical landslides as case studies for deformation enhancement, it is verified that the method maintains the original deformation characteristics while reducing noise and has its unique methodological advantages. It should be noted that the abovementioned successes are in mountainous areas with neighboring spatial similarities. From the perspective of the method principle of deformation enhancement, it is not advantageous in urban areas with complex features. This is a research direction that we need to further validate and optimize in the future.

Stability assessment of the landslide surface based on the results of deformation enhancement. According to the deformation differences between spatially adjacent monitoring points, the angular distortions are calculated, potential landslides are discovered, and the possible external edges of the landslide body are mapped. By combining optical image observation with angular distortions, the spatial deformation characteristics of the landslide surface are analyzed, overcoming the limitations of traditional stability assessment based only on velocity. In addition, through the PCA method, the main component information is concentrated, and it is found that the first principal component is most closely related to the distribution characteristics of surface deformation, with strong spatial consistency. Furthermore, the surface deformation drivers of landslide areas are discussed in terms of geological factors and triggering conditions, and seasonal precipitation is considered to be one of the main influencing factors at present.

The InSAR deformation enhancement method and stability assessment strategy proposed can provide a more comprehensive understanding of the deformation pattern of landslides in mountainous areas, which is of value as a reference and guide for disaster mitigation and prevention.

Acknowledgment

Youfeng Liu, Honglei Yang, and Runcheng Jiao conceived the original design of this article. Youfeng Liu and Honglei Yang improve the structure of this article. Zeping Wang, Jianfeng Han, Wei Zeng, and Liuyu Wang provided comments on this article. All authors have read and agreed to the published version of the manuscript. The authors would like to thank the Canadian Space Agency for providing RADARSAT-2 data.

References

[1] M. Li et al., "Retrieval of historical surface displacements of the Baige landslide from time-series SAR observations for retrospective analysis of the collapse event," *Remote Sens. Environ.*, vol. 240, Apr. 2020, Art. no. 111695.

[2] D. Jin et al., "Interferometric synthetic aperture radar applicability analysis for potential landslide identification in steep mountainous areas with C/L band data," *Remote Sens.*, vol. 15, Sep. 2023, Art. no. 4538.

[3] K. Ya, Z. Lu, C. Zhao, and W. Qu, "Inferring slip-surface geometry and volume of creeping landslides based on InSAR: A case study in Jinsha River basin," *Remote Sens. Environ.*, vol. 294, May 2023, Art. no. 113620.

[4] Z. Zhang, Q. Zeng, and J. Jiao, "Deformations monitoring in complicated-surface areas by adaptive distributed scatterer InSAR combined with land cover: Taking the Jiaju landslide in Danba, China as an example," *ISPRS J. Photogrammetry Remote Sens.*, vol. 186, pp. 102–122, Apr. 2022.

[5] R. Jiao et al., "Comprehensive remote sensing technology for monitoring landslide hazards and disaster chain in the Xishan mining area of Beijing," *Remote Sens.*, vol. 14, Oct. 2022, Art. no. 4695.

[6] Y. Zhang et al., "Forecasting the magnitude of potential landslides based on InSAR techniques," *Remote Sens. Environ.*, vol. 241, May 2020, Art. no. 111738.

[7] B. Benedikt, A. Simoni, M. Mulas, A. Corsini, and D. Schmidt, "Deformation responses of slow moving landslides to seasonal rainfall in the Northern Apennines, measured by InSAR," *Geomorphology*, vol. 308, pp. 293–306, May 2018.

[8] A. Ferretti, C. Prati, and F. Rocca, "Nonlinear subsidence rate estimation using permanent scatterers in differential SAR interferometry," *IEEE Trans. Geosci. Remote Sens.*, vol. 38, no. 5, pp. 2202–2212, Sep. 2000.

[9] A. Hooper et al., "Recent advances in SAR interferometry time series analysis for measuring crustal deformation," *Tectonophysics*, vol. 514, pp. 1–13, Jan. 2012.

[10] K. Goel and N. Adam, "A distributed scatterer interferometry approach for precision monitoring of known surface deformation phenomena," *IEEE Trans. Geosci. Remote Sens.*, vol. 52, no. 9, pp. 5454–5468, Sep. 2014.

[11] G. Fornaro, S. Verde, D. Reale, and A. Pauciullo, "CAESAR: An approach based on covariance matrix decomposition to improve multibaseline–multitemporal interferometric SAR processing," *IEEE Trans. Geosci. Remote Sens.*, vol. 53, no. 4, pp. 2050–2065, Apr. 2015.

[12] B. Osmanoğlu et al., "Time series analysis of InSAR data: Methods and trends," *ISPRS J. Photogrammetry Remote Sens.*, vol. 115, pp. 90–102, May 2016.

[13] H. Wu et al., "SAR interferometry on full scatterers: Mapping ground deformation with ultra-high density from space," *Remote Sens. Environ.*, vol. 302, 2024, Art. no. 113965.

[14] P. Berardino, G. Fornaro, R. Lanari, and E. Sansosti, "A new algorithm for surface deformation monitoring based on small baseline differential SAR interferograms," *IEEE Trans. Geosci. Remote Sens.*, vol. 40, no. 11, pp. 2375–2383, Nov. 2002.
[15] L. Zhang, X. Ding, and Z. Lu, "Ground settlement monitoring based on temporarily coherent points between two SAR acquisitions," *ISPRS J. Photogrammetry Remote Sens.*, vol. 66, no. 1, pp. 146–152, Jan. 2011.
[16] A. Ferretti, A. Fumagalli, F. Novali, C. Prati, and A. Rucci, "A new algorithm for processing interferometric data-stacks: SqueeSAR," *IEEE Trans. Geosci. Remote Sens.*, vol. 49, no. 9, pp. 3460–3470, Sep. 2011.
[17] A. Abir et al., "Active tectonics of Western Potwar Plateau–Salt Range, Northern Pakistan from InSAR observations and seismic imaging," *Remote Sens. Environ.*, vol. 168, pp. 265–275, Oct. 2015.
[18] J. Cai et al., "Detection and characterization of slow-moving landslides in the 2017 Jiuzhaigou earthquake area by combining satellite SAR observations and airborne Lidar DSM," *Eng. Geol.*, vol. 305, Aug. 2022, Art. no. 106730.
[19] X. Hu, R. Bürgmann, Z. Lu, A. Handwerger, T. Wang, and R. Miao, "Mobility, thickness, and hydraulic diffusivity of the slow-moving Monroe landslide in California revealed by L-band satellite radar interferometry," *J. Geophysical Res.-Solid Earth*, vol. 124, pp. 7504–7518, Jul. 2019.
[20] W. Janusz and F. Bovenga, "Investigating landslides and unstable slopes with satellite multi temporal interferometry: Current issues and future perspectives," *Eng. Geol.*, vol. 174, pp. 103–138, May 2014.
[21] J. Wang et al., "Monitoring of large-scale landslides in Zongling, Guizhou, China, with improved distributed scatterer interferometric SAR time series methods," *Landslides*, vol. 17, pp. 1777–1795, Aug. 2020.
[22] J. Bao et al., "An improved distributed scatterers extraction algorithm for monitoring tattered ground surface subsidence with DSInSAR: A case study of loess landform in Tongren county," *Int. J. Appl. Earth Observ. Geoinf.*, vol. 99, Jul. 2021, Art. no. 102322.
[23] H. Chen, C. Zhao, B. Li, Y. Gao, L. Chen, and D. Liu, "Monitoring spatiotemporal evolution of Kaiyang landslides induced by phosphate mining using distributed scatterers InSAR technique," *Landslides*, vol. 20, pp. 695–706, Mar. 2023.
[24] Z. Xia, M. Motagh, T. Li, M. Peng, and S. Roessner, "A methodology to characterize 4D post-failure slope instability dynamics using remote sensing measurements: A case study of the Aniangzhai landslide in Sichuan, Southwest China," *ISPRS J. Photogrammetry Remote Sens.*, vol. 196, pp. 402–414, Feb. 2023.
[25] X. Liu et al., "Integration of Sentinel-1 and ALOS/PALSAR-2 SAR datasets for mapping active landslides along the Jinsha River corridor, China," *Eng. Geol.*, vol. 284, Apr. 2021, Art. no. 106033.
[26] C. Pascal, J. Garfias, R. Martel, C. Brouard, and A. Rivera, "InSAR to support sustainable urbanization over compacting aquifers: The case of Toluca Valley, Mexico," *Int. J. Appl. Earth Observ. Geoinf.*, vol. 63, pp. 33–44, Dec. 2017.
[27] C. Francesca and D. Tapete, "Present-day land subsidence rates, surface faulting hazard and risk in Mexico City with 2014–2020 Sentinel-1 IW InSAR," *Remote Sens. Environ.*, vol. 253, Feb. 2021, Art. no. 112161.
[28] L. Gunnar, "Non-linear visualization and analysis of large water quality data sets: A model-free basis for efficient monitoring and risk assessment," *Stochastic Environ. Res. Risk Assessment*, vol. 23, pp. 977–990, Oct. 2009.
[29] C. Estelle, R. Bürgmann, M. Shirzaei, E. Fielding, and B. Baker, "Predictability of hydraulic head changes and characterization of aquifer-system and fault properties from InSAR-derived ground deformation," *J. Geophysical Res.-Solid Earth*, vol. 119, pp. 6572–6590, Aug. 2014.
[30] G. Shi, P. Ma, X. Hu, B. Huang, and H. Lin, "Surface response and subsurface features during the restriction of groundwater exploitation in Suzhou (China) inferred from decadal SAR interferometry," *Remote Sens. Environ.*, vol. 256, Apr. 2021, Art. no. 112327.
[31] Y. Liu, H. Yang, S. Wang, L. Xu, and J. Peng, "Monitoring and stability analysis of the deformation in the Woda landslide area in Tibet, China by the DS-InSAR method," *Remote Sens.*, vol. 14, no. 3, Feb. 2022, Art. no. 532.
[32] X. Hu, R. Bürgmann, W. Schulz, and E. Fielding, "Four-dimensional surface motions of the Slumgullion landslide and quantification of hydrometeorological forcing," *Nature Commun.*, vol. 11, Jun. 2020, Art. no. 2792.
[33] C. Pu et al., "Refined mapping and kinematic trend assessment of potential landslides associated with large-scale land creation projects with multi-temporal InSAR," *Int. J. Appl. Earth Observ. Geoinf.*, vol. 118, Apr. 2023, Art. no. 103266.
[34] Y. Wang et al., "Automatic detection and update of landslide inventory before and after impoundments at the Lianghekou reservoir using Sentinel-1 InSAR," *Int. J. Appl. Earth Observ. Geoinf.*, vol. 118, Apr. 2023, Art. no. 103224.
[35] G. Shi, H. Lin, R. Bürgmann, P. Ma, J. Wang, and Y. Liu, "Early soil consolidation from magnetic extensometers and full resolution SAR interferometry over highly decorrelated reclaimed lands," *Remote Sens. Environ.*, vol. 231, Sep. 2019, Art. no. 111231.
[36] Y. Liu, H. Yang, J. Fan, J. Han, and Z. Lu, "NL-MMSE: A hybrid phase optimization method in multimaster interferogram stack for DS-InSAR applications," *IEEE J. Sel. Topics Appl. Earth Observ. Remote Sens.*, vol. 15, pp. 8332–8345, 2022.
[37] M. Jiang and A. M. Guarnieri, "Distributed scatterer interferometry with the refinement of spatiotemporal coherence," *IEEE Trans. Geosci. Remote Sens.*, vol. 99, no. 6, pp. 3977–3987, Jun. 2020.
[38] H. Fan et al., "Surface subsidence monitoring with an improved distributed scatterer interferometric SAR time series method in a filling mining area," *Geocarto Int.*, vol. 37, no. 25, pp. 8979–9001, Dec. 2022.
[39] V. Dalia, R. Lillo, and J. Romo, "A Kendall correlation coefficient between functional data," *Adv. Data Anal. Classification*, vol. 13, pp. 1083–1103, Dec. 2019.
[40] U. Alexandra, A. Handwerger, M. Bakker, and T. Bogaard, "A new method to detect changes in displacement rates of slow-moving landslides using InSAR time series," *Landslides*, vol. 19, pp. 2233–2247, Jun. 2022.
[41] M. Jiang, X. Ding, R. F. Hanssen, R. Malhotra, and L. Chang, "Fast statistically homogeneous pixel selection for covariance matrix estimation for multitemporal InSAR," *IEEE Trans. Geosci. Remote Sens.*, vol. 53, no. 3, pp. 1213–1224, Mar. 2015.
[42] M. Jiang et al., "The potential of more accurate InSAR covariance matrix estimation for land cover mapping," *ISPRS J. Photogrammetry Remote Sens.*, vol. 126, pp. 120–128, Apr. 2017.

Youfeng Liu received the B.S. degree in surveying and mapping engineering from Henan Polytechnic University, Jiaozuo, China, in 2018, and the M.S. degree in geodesy from the China University of Mining and Technology, Xuzhou, China, in 2021. Since 2021, he has been working toward the Ph.D. degree in surveying and mapping science and technology with the School of Land Science and Technology, China University of Geosciences, Beijing, China.

His research interests include satellite and ground-based InSAR data processing and its application in surface deformation monitoring.

Honglei Yang was born in 1983. He received the Ph.D. degree in cartography and geographical information engineering from the China University of Geosciences, Beijing, China, in 2012.

Since 2014, he has been teaching with the China University of Geosciences, where he currently serves as a Professor and Ph.D. supervisor. He is engaged in scientific research in the fields of satellite and ground-based InSAR data processing, microwave remote sensing data processing theory and application, etc. He has presided over and participated in the projects of the National Natural Science Foundation of China, the Key Research and Development Program of the Ministry of Science and Technology, the China–Europe Dragon Project, etc. He has authored or coauthored more than 30 papers.

Runcheng Jiao received the master's degree in remote sensing of resources and environment from China University of Geosciences, Beijing, China, in 2010. Since 2023, he has been working toward the Ph.D. degree in surveying and mapping science and technology with the School of Land Science and Technology, China University of Geosciences, Beijing, China.

He currently holds the position of Professor-Level Senior Engineer with the Beijing Institute of Geological Disaster Prevention and Control, Beijing, China, where he serves as the Head of the Remote Sensing Information Center. Additionally, he is a Postgraduate Supervisor with the China University of Geosciences, a Visiting Professor with the Inner Mongolia University of Science and Technology, and a Team Leader with the Geological Disaster Monitoring and Prevention Innovation Base of Geological Society of China. His research interests focus on remote sensing geology and geological disaster research.

Zeping Wang received the B.S. degree in surveying and mapping engineering from Henan Polytechnic University, Jiaozuo, China, in 2021. Since 2022, he has been working toward the Ph.D. degree in surveying and mapping science and technology with the School of Land Science and Technology, China University of Geosciences, Beijing, China.

His research interests are the development and application of InSAR algorithms.

Liuyu Wang received the B.S. degree in surveying and mapping engineering and the Ph.D. degree in geodesy and survey engineering from the China University of Mining and Technology, Xuzhou, China, in 2014 and 2020, respectively.

Her research interests focus on time-series InSAR analysis and deformation monitoring.

Wei Zeng received the master's degree in land resource management from East China University of Technology, Nanchang, China, in 2012.

He is currently working with the Chinese Society for Geodesy Photogrammetry and Cartography, Beijing, China. He has long been engaged in the research of 3S technology in sustainable land use and development.

Jianfeng Han received the B.S. degree in surveying engineering and the M.S. degree in surveying and mapping from the China University of Geosciences, Beijing, China, in 2019 and 2022, respectively.

Since 2022, he has been working with the Beijing Institute of Geological Hazard Prevention. Beijing, China. His main research area is remote sensing monitoring.